Supplementary Materials for

Nanoparticle Exsolution via Electrochemical Switching in Perovskite Fibers for Solid Oxide Fuel Cell electrodes

Min Xu[1,2,3*], Ran Cao[1,4], Shitao Wu[3], JinGoo Lee[5], Di Chen[1], John T.S. Irvine[3*]

[1]The Future Laboratory, Tsinghua University, Beijing, 100084, China

[2]Academy of Arts & Design, Tsinghua University, Beijing 100084, China

[3]School of Chemistry, University of St Andrews, St Andrews, KY16 9ST, U.K.

[4]Weiyang College, Tsinghua University, Beijing, 100084, China

[5]Advanced Energy Materials and Components R&D Group, Dongnam Division, Korea Institute of Industrial Technology, 33-1, Jungang-ro, Yangsan, Gyeongsangnam-do, 50623, Republic of Korea

*Correspondence to: xumin2022@mail.tsinhua.edu.cn, jtsi@st-andrews.ac.uk.

This PDF file includes:

1. Experimental

1.1 Synthesis of LCNT samples

For the LCNT fibers, Lanthanum chloride heptahydrate ($LaCl_3 \cdot 6H_2O$, 99%, Alfa Aesar), Calcium chloride ($CaCl_2$, Fisher Scientific), Nickel chloride hexahydrate ($NiCl_2 \cdot 6H_2O$, 99.9%, Alfa Aesar), Titanium (IV) isopropoxide ($C_{12}H_{20}O_4Ti$, 97%, Sigma-Aldrich) and Polyvinylpyrrolidone (PVP, M.W.=1,300,000, Alfa Aesar) were used as raw materials. For the powder sample prepared by solid-state reaction, Lanthanum oxide (La_2O_3, 99.99%, Pi-KEM), Calcium chloride ($CaCO_3$, 99.5%, Alfa Aesar), and Nickel nitrate hexahydrate ($Ni(NO_3)_2 \cdot 6H_2O$, 99%, Acros) were used. All the regents were used as received without further treatments.

LCNT fibers were prepared via the electrospinning method. Stoichiometric amounts of salts and PVP were dissolved in a mixture of ethanol and acetic acid as solvent (volume ratio 2:1). The acetic acid here acts as a stabilizer to control the hydrolysis reaction of the sol-gel precursor. The concentration of the salts was 0.2 M in the precursor solution. The PVP in the metal solution was kept at a weight ratio of 2.5 wt% to reach a viscosity for achieving an appropriate polymer entanglement by the electric field. The solution was loaded into a plastic syringe (5 mL) with a stainless-steel spinneret (D ¼ 0.5 mm). The supply rate of the precursor in the electrospinning set-up was 0.3 mL h^{-1}. A 12 kV voltage was applied between a spinneret and an aluminum foil collector at a distance of 10 cm. The electrospun nanofibers were peeled off from the collector, then dried at 80 °C for 5 h followed by calcination at 1100 °C for 2 h to form the pure perovskite phase. The as-prepared perovskite samples were further treated in 5 % H_2/Ar to obtain the reduced samples.

The samples prepared by solid-state reaction were used as the control group. The dried raw materials were weighted in an appropriate stoichiometric ratio and followed by suitable mixing with acetone by the ultrasonic probe. The homogenous mixture was dried overnight with stirring

to obtain a uniform powder. This powder was transferred to the furnace and pre-calcined at 1000 ℃ for 12 h to decompose carbonate and to achieve the perovskite nucleation. The calcined powder then undergoes ball milling to achieve good mixing and is pressed into the pellet followed by calcination at 1400 ℃ for 12 h.

1.2 Cell preparation and measurements

Electrolyte-supported cells were fabricated to test the electrochemical performance of electrodes. LCNT fiber slurries were prepared by grounding the material with ethyl cellulose in terpineol for 1 h. $(La_{0.8}Sr_{0.2})_{0.95}MnO_3$ (Pi-KEM) and 8YSZ (Pi-KEM) in a 50:50 ratio were dispersed by roller milling with the addition of acetone and hypermer KD1 (2 wt%) overnight to prepare the air electrode slurry. Electrode slurries were brush-painted on both surfaces of 200 μm thick YSZ discs and calcined at 1100 ℃ for 2 h to bond the electrodes with the electrolyte. The electrode area is about 0.28 cm^2.

The electrolyte-supported cell was sealed on the alumina tube using ceramic sealant (AREMCO 552). The conductive gold paste (METALOR) was used as current collector and coated on the surface of the electrode, followed by heating at 750 ℃ for 1 h to remove the organic compounds. Gold wires were used to connect the cell to the electrochemistry station (Solartron 1280B). The purged hydrogen in the anode side were controlled by mass flow controllers with a flow rate of 20 ml min^{-1}, and the air side was exposed to stationary air. The cell was heated at various temperatures for 20 min to maintain a constant temperature. AC impedance data of the cells were collected via electrochemical impedance spectra (EIS) using an electrochemical workstation with 10 mV amplitude at open circuit voltage (OCV) and a frequency range from 10^{-1} Hz to 10^6 Hz. For IV test, the sweep voltammetry was scanned with a rate of 20 mV s^{-1} for all

tests. The galvanostatic potential was used to impose constant bias (from 1.8 to 2.1 V) versus the air electrode on the cell and to achieve electrochemical switching.

1.3 Characterization

Powder X-ray diffraction (PXRD) measurements were performed at room temperature on representative samples with an X-ray angle from 10-90 ° by using a PANalytical Empyrean diffractometer with Cu Kα1 radiation (1.54056 Å) and Bragg-Brentanon geometry operating in reflection mode. FEI Scios electron microscope was used to acquire high-resolution images for investigating the morphology of nanofibers and the exsolution of nanoparticles. The number and diameter/size of the fibers/particles were calculated from the adequately magnified images. To analyze the microstructure of the nanoparticles on the sample, TEM and elected area diffraction (SAD) images were taken with a JEOL JEM-2011 transmission electron microscope. The specimens for TEM were first ground using a mortar and a pestle then dispersed in acetone before loading on a copper grid with supportive carbon films.

Thermo-gravimetric analysis (TGA) measurements for exsolution investigation were performed on a NETZSCH STA 449 C instrument using Proteus thermal analysis software. The initial weight of the samples was about 40 mg. The mass was recorded when heated to 800 ℃ under corresponding chemical reduction in a gas atmosphere flowing 5% H_2/Ar (30 ml min^{-1}), with a heating rate of 5 ℃ min^{-1}. Thereafter, an isothermal procedure was carried out for 10 h at 800 ℃. The blank weight change reference with an empty crucible was recorded under the same conditions and subtracted from the sample data. The raw data were numerically differentiated to obtain differential thermogravimetry curves.

Specific surface area (S_{BET}), average pore volume and pore size of the prepared samples were determined by the distribution graph of N_2 adsorption-desorption at 77 K using Micromeritics

TRISTAR II 2020. Samples are outgassed at 200 ℃ under vacuum for 12 h using a Quantachrome Flovac degasser (Micromeritics VacPrep 061). N_2 isothermal data sets were collected at -195 ℃. S_{BET} was calculated by the Brunauer-Emmett-Teller multiple point method at partial pressure range from 0.05 to 0.3. Total pore volumes were determined at p/p_0=0.99.

The X-ray absorption near edge spectrum (XANES) of the Ni K (8.3330 KeV) edge for selected samples was collected at ambient temperature on the B18 station at Diamond Light Source national synchrotron facility, UK. The absorption near the Ni K edges was determined from the total transmission yield. Measurements were carried out using a Si(111) monochromator with a Ni monometallic foil (10 μm) used as an energy calibrant prior to measurement. Samples were pressed into 13 mm pellets and diluted using the appropriate amount of cellulose binder. Ni foil and $Ni(NO_3)_2$ were used as references for Ni^0 and Ni^{2+}, respectively. The data were analyzed using Athena from the Deserter suite, which implements the FEFF6 and IFEFFIT codes and Artemis.[1,2]

1.4 Model description and phase-field theory

The model for the exsolution behavior on A-site deficient perovskite was derived in a thermodynamically consistent manner by combining a ternary regular-solution free energy functional and Cahn-Hilliard kinetic equations. The exsolution as a phase transformation process involved three steps: segregation in the surface region, spinodal decomposition (nucleation) and coarsening (growth) of B-site metal particles. To understand the possible mechanism of electrochemically driven exsolution, the phase-field model describes the kinetics and microstructure evolution was implemented by COMSOL Multiphysics (5.5). Detailed geometry and functional parameters with dimensionless units were summarized in Table S1.

The exsolution of perovskite fiber (as a solid solution material) can be treated as a three phases system, including perovskite matrix, reduction gas atmosphere and nanoparticles (Fig.5(a)). The

exsolution can be explained by a thermodynamic regular-solution model[3] by considering the homogeneous Gibbs free energy per mole of the perovskite system:

$$g = \sum_{i=P,B\prime,A} \{[\mu_i^0 + (1-\eta^2)\mu_i^{seg}]x_i + x_i RT \ln x_i + \sum_{i=P,B\prime,A} \sum_{j>i} x_i x_j L_{ij} \quad \text{Eq.S1}$$

where i are the components including perovskite (P), B site dopant (B') and atmosphere (A), x represents the molar fractions of components, R is the gas constant, T is the temperature of the system. Here, η as the structural order parameter (η = 1 in the perovskite and η = -1 in the atmosphere, and smooth transition of η between 1 and -1 in the metastable region) was used to define the difference of components. M_i^0 indicates the standard chemical potential of components. The decreased standard chemical potential of B' in the surface region than the bulk have been proved by DFT calculations.[4,5] Therefore, the driving force of exsolution can be defined as chemical potential difference, i.e. the segregation energy $\mu_{B\prime}^{seg} = \mu_{B\prime}^0(surface) - \mu_{B\prime}^0(bulk)$. $L_{ij}(pO_2)$ represents the implicit relationship between pO_2 and interaction energies between components i and j, which can be increased by decreasing pO_2. The interaction parameter L_{ij} should be positive to create a desired equilibrium composition of atmosphere, perovskite, and nanoparticles and their metastable and spinodal state.[3]

According to Cahn-Hilliard model for heterogeneous systems, the free energy depends on local free energy and the gradient energy coefficients can be expressed as:

$$G = \int_V [g + \sum_{i=P,B\prime,A} \frac{\kappa_i}{2} (\nabla x_i)^2] dV \quad \text{Eq.S2}$$

where κ_i is the gradient energy coefficient. For the perovskite exsolution system, two degree of freedom are considered as $x_P + x_{B\prime} + x_A = 1$. The spatial and temporal kinetic evolution of x_P and $x_{B\prime}$ were evaluated by the Cahn-Hilliard equations:

$$\partial \mathrm{x}_P / \partial \mathrm{t} = \nabla \cdot (\mathrm{M}_P \nabla \mu_P) \quad \text{Eq.S3}$$

$$\partial \mathrm{x}_{\mathrm{B}'} / \partial \mathrm{t} = \nabla \cdot (\mathrm{M}_{\mathrm{B}'} \nabla \mu_{\mathrm{B}'}) \quad \text{Eq.S4}$$

where $\mathrm{M_P}$ and $\mathrm{M_B}$, are the Onsager coefficients related to diffusion coefficients. μ_P and μ_B, can be given from Euler-Lagrange equations:

$$\mu_P = \delta G / \delta x_P = \partial g / \partial x_P - (\kappa_P + \kappa_A)\nabla^2 x_P - \kappa_A \nabla^2 x_{B'} \quad \text{Eq.S5}$$

$$\mu_{B'} = \delta G / \delta x_{B'} = \partial g / \partial x_{B'} - (\kappa_{B'} + \kappa_A)\nabla^2 x_{B'} - \kappa_A \nabla^2 x_P \quad \text{Eq.S6}$$

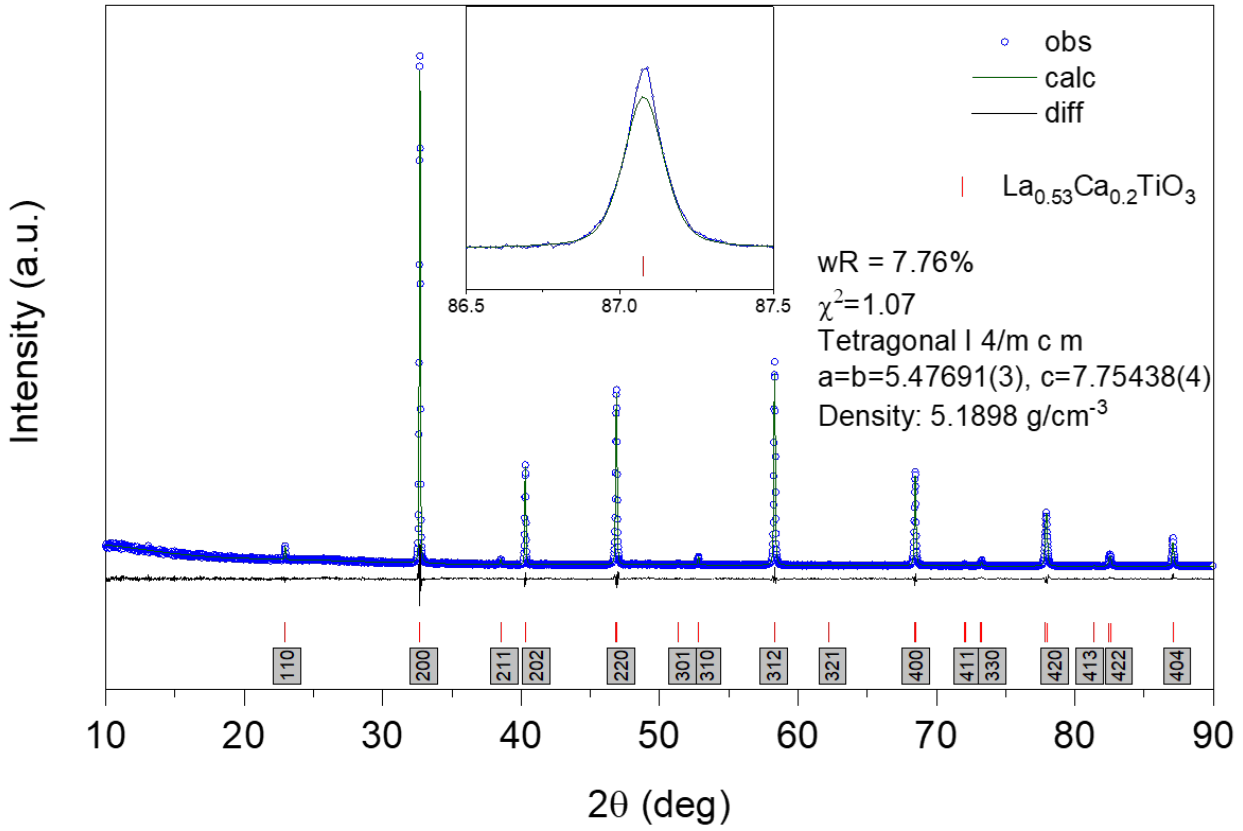

Figure S1. Rietveld refinement for LCNT powder sample. Miller indices are shown in the figure. The Bragg positions of reference $La_{0.53}Ca_{0.2}TiO_3$ (ICSD_CollCode245544) is list in the figure.

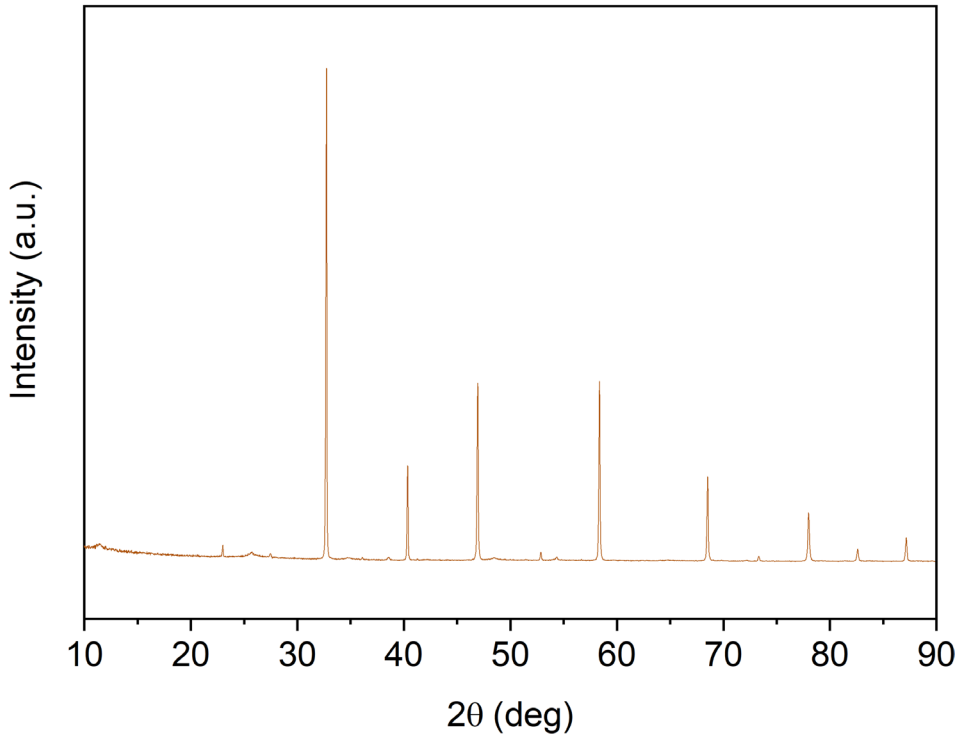

Figure S2. XRD pattern of $La_{0.52}Ca_{0.28}Ni_{0.03}Ti_{0.97}O_3$ fibers sample.

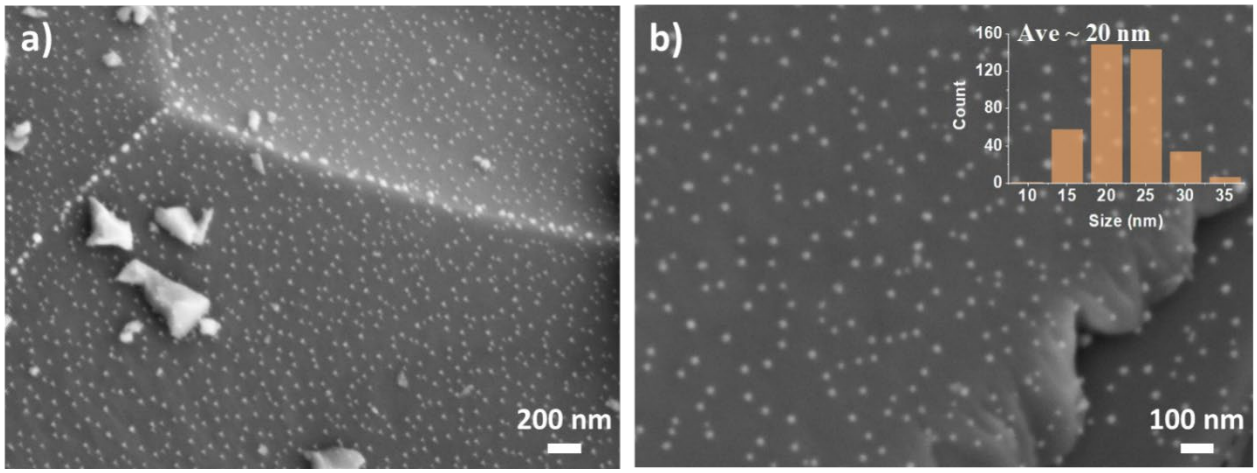

Figure S3. LCNT samples were calcined at 1100 ℃ subsequently reduced at 900 ℃ for 4 h in 5% H_2/N_2.

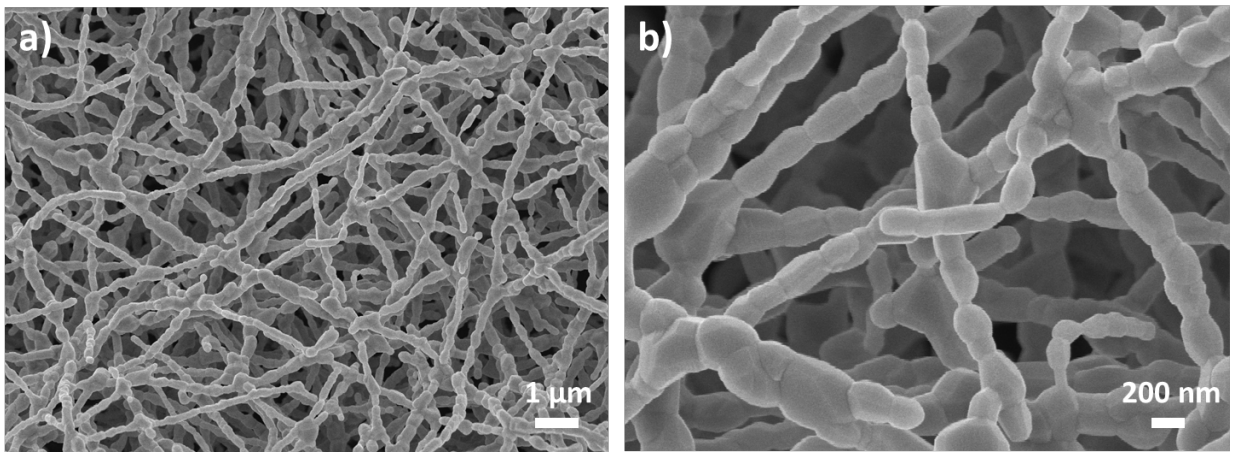

Figure S4. High resolution SEM images of LCNT fibres calcined in air.

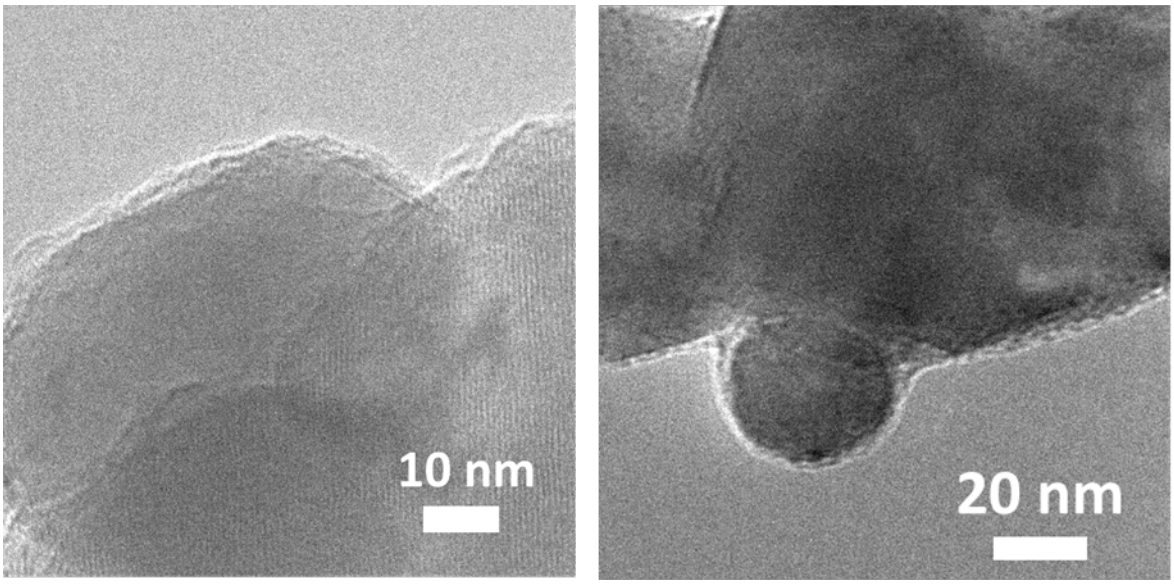

Figure S5. TEM images of exsolved particles with various embed depth.

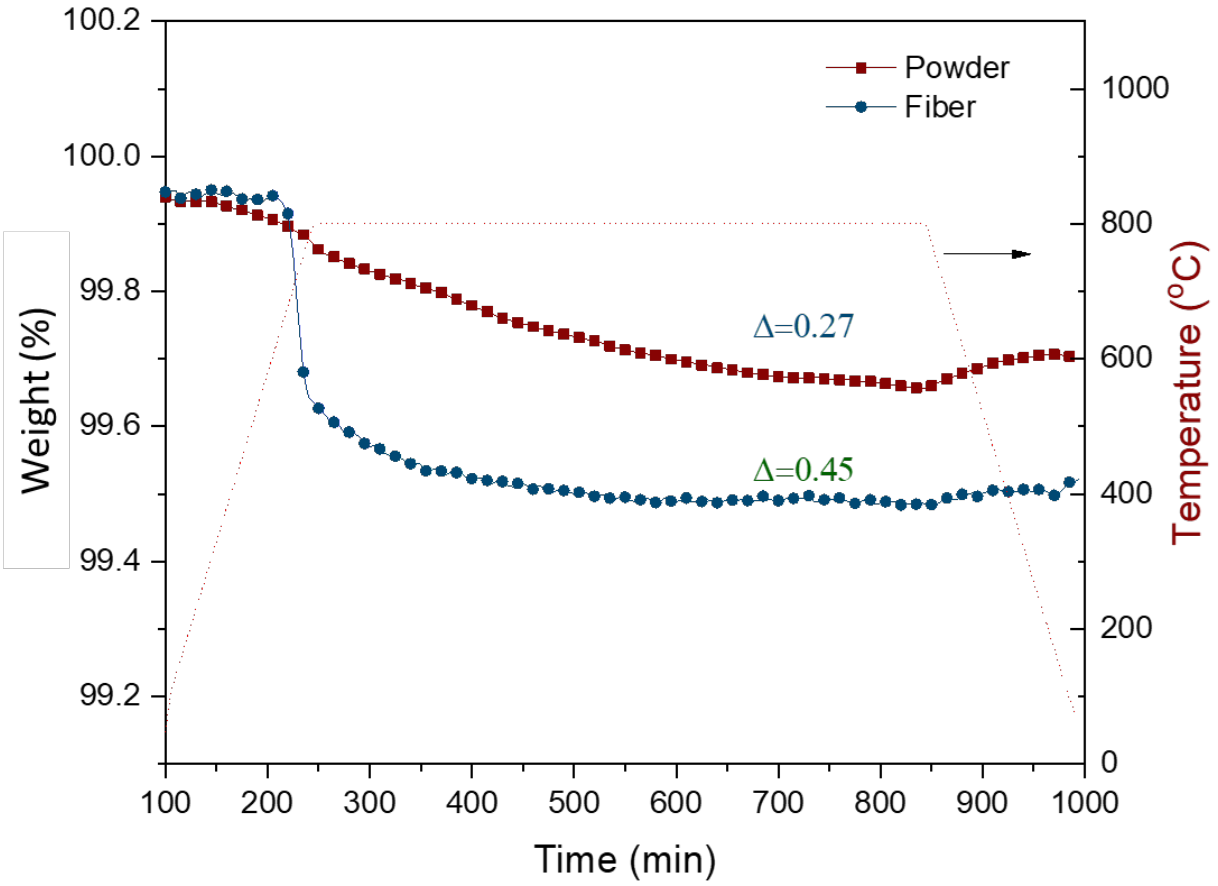

Figure S6. LCNT samples were calcined at 1100 ℃ subsequently isothermally reduced at 800 ℃ for 10 h in 5% H_2/N_2. The weight loss is plotted vs time.

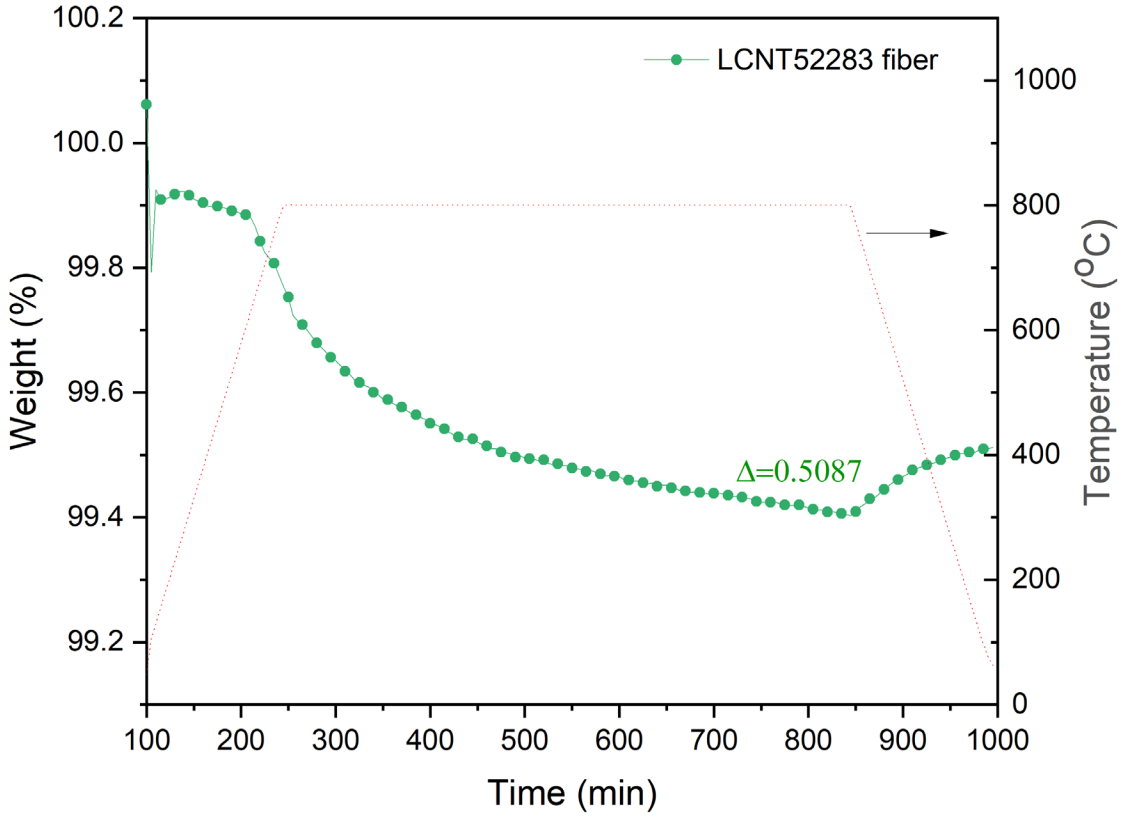

Figure S7. $La_{0.52}Ca_{0.28}Ni_{0.03}Ti_{0.97}O_3$ fiber samples were calcined at 1100 ℃ subsequently isothermally reduced at 800 ℃ for 10 h in 5% H_2/N_2. The weight loss is plotted vs time.

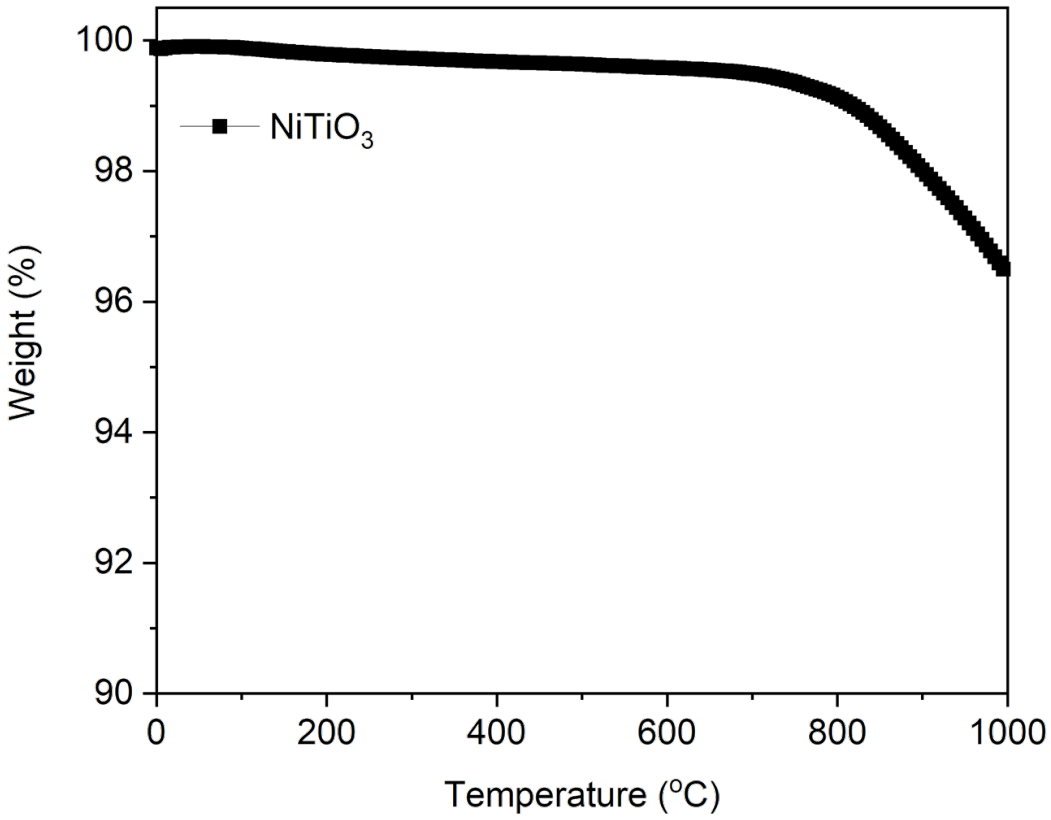

Figure S8. $NiTiO_3$ samples were reduced upto 800 ℃ in 5% H_2/N_2.

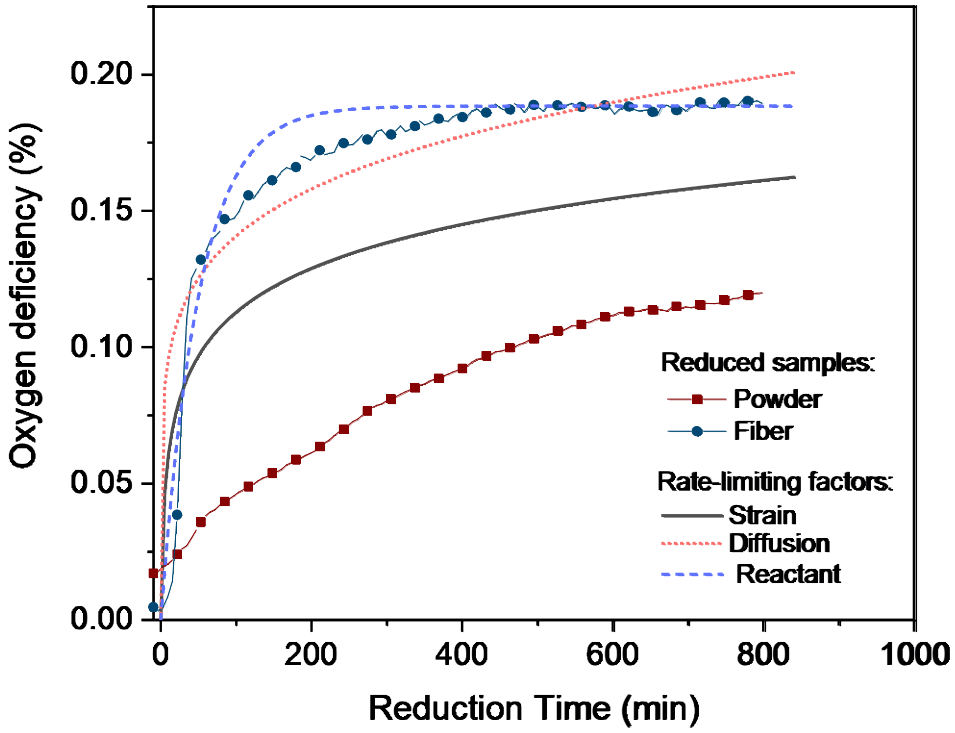

Figure S9. Model analysis of the rate-limiting factors of the formation of oxygen deficiency with time.

Three limiting factors that may determine the rate of the reduction (related to the growth of exsolution particles) are discussed, including (i) strain caused interaction between metal and host, (ii) available concentration of the reactant (oxygen anion or resolvable cation) and (iii) the diffusion of the ions to the surface.[6] In these equations, d and t denote oxygen deficiency and time; d and τ are fitting parameters. The rate-limiting models can be expressed as[6]:

Strain-limited kinetics

$$\delta = \delta_{0,s}\left(ln\left(1+\frac{t}{\tau_s}\right)\right)^{\frac{1}{3}} \quad \text{Eq.S7}$$

Reactant-limited kinetics

$$\delta = \delta_{0,r}\left(1-e^{\left(-\frac{t}{\tau_r}\right)}\right)^{\frac{1}{3}} \quad \text{Eq.S8}$$

Diffusion-limited kinetics

$$\delta = \delta_{0,d}\left(\frac{t}{\tau_d}\right)^{\frac{1}{6}} \quad \text{Eq.S9}$$

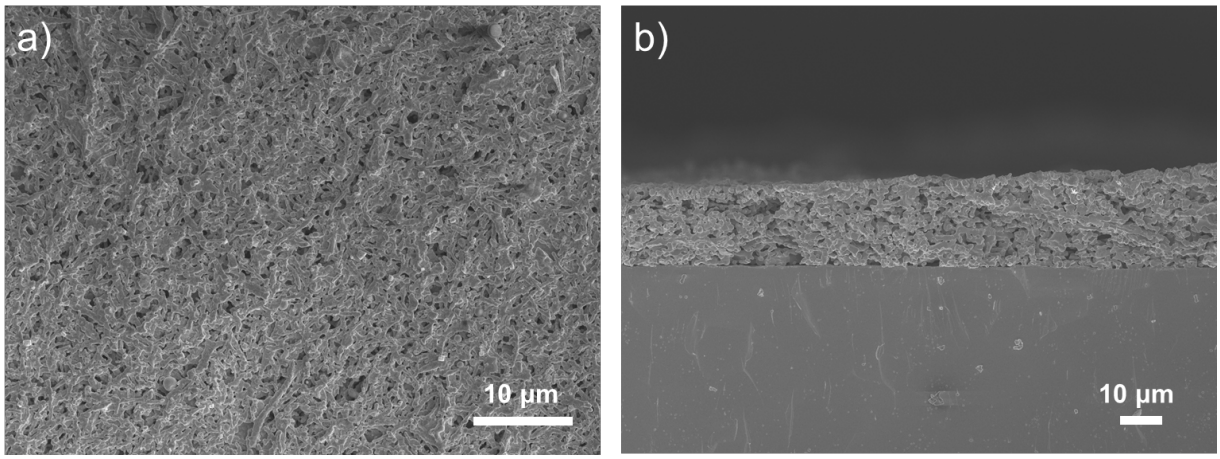

Figure S10. Morphology of exsolution on fiber electrode in symmetrical cell reduced at 800 ℃ in 5% H_2/N_2 for 2 h. (a) surface and (b) cross section.

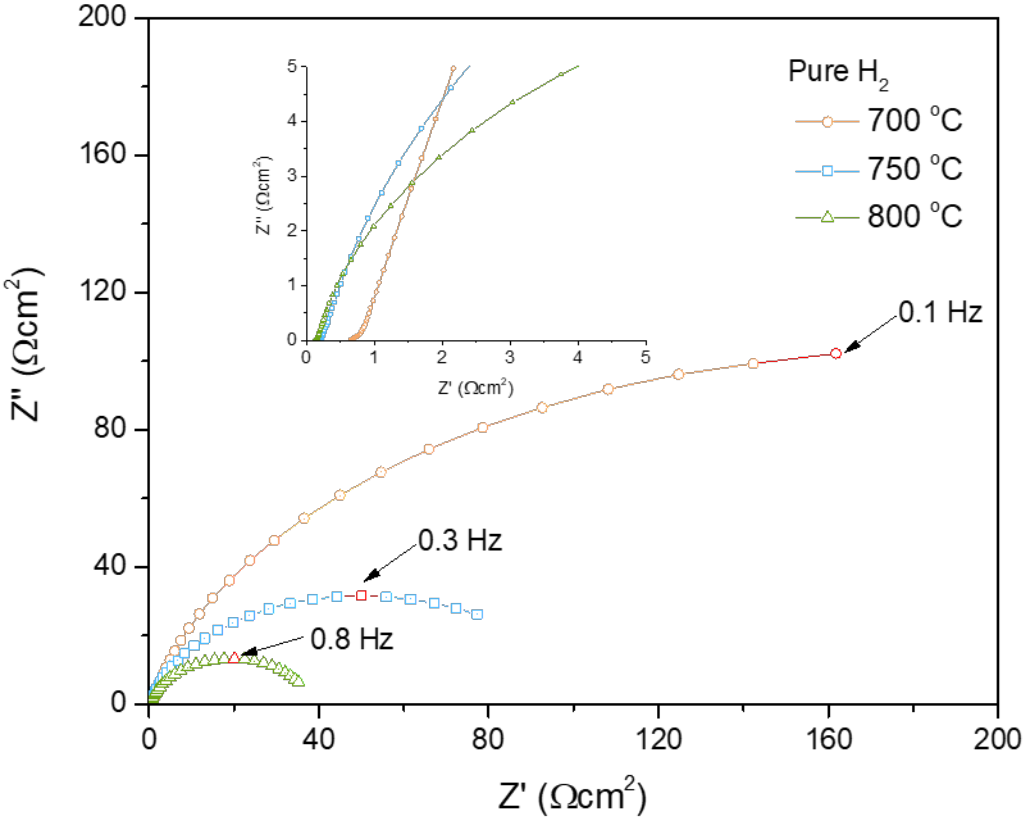

Figure S11. AC impedance spectra of the symmetric fiber-based cell reduced in pure hydrogen. The inset figures are the corresponding zoom in the area to display the intercept of impedance and SEM image of the cross-section of the cell. The R_p of the symmetric cell is further reduced to about 40 Ω cm^2. The R_p of symmetrical cells depends on the measured temperature due to the sluggish activity of exsolution at low temperatures.

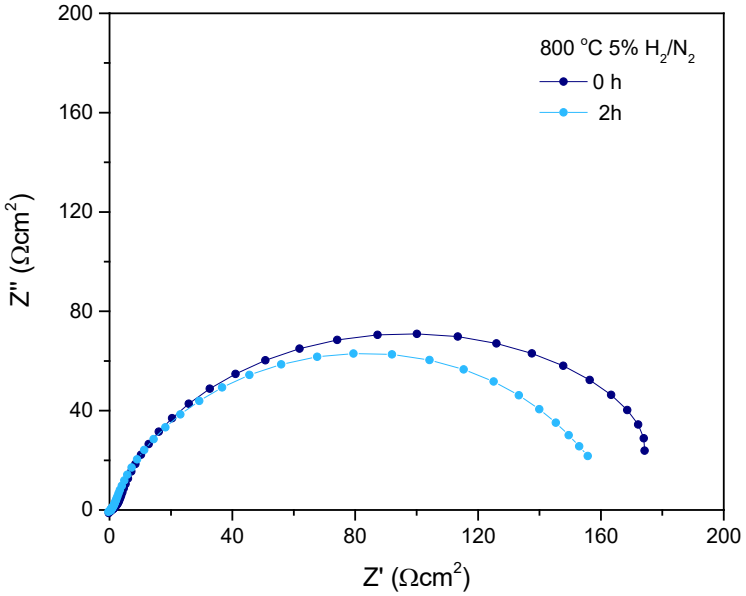

Figure S12. Impedance spectra of the powder electrode symmetric cell reduced at 800 ℃ in 5% H_2/N_2 for 0 and 2 h.

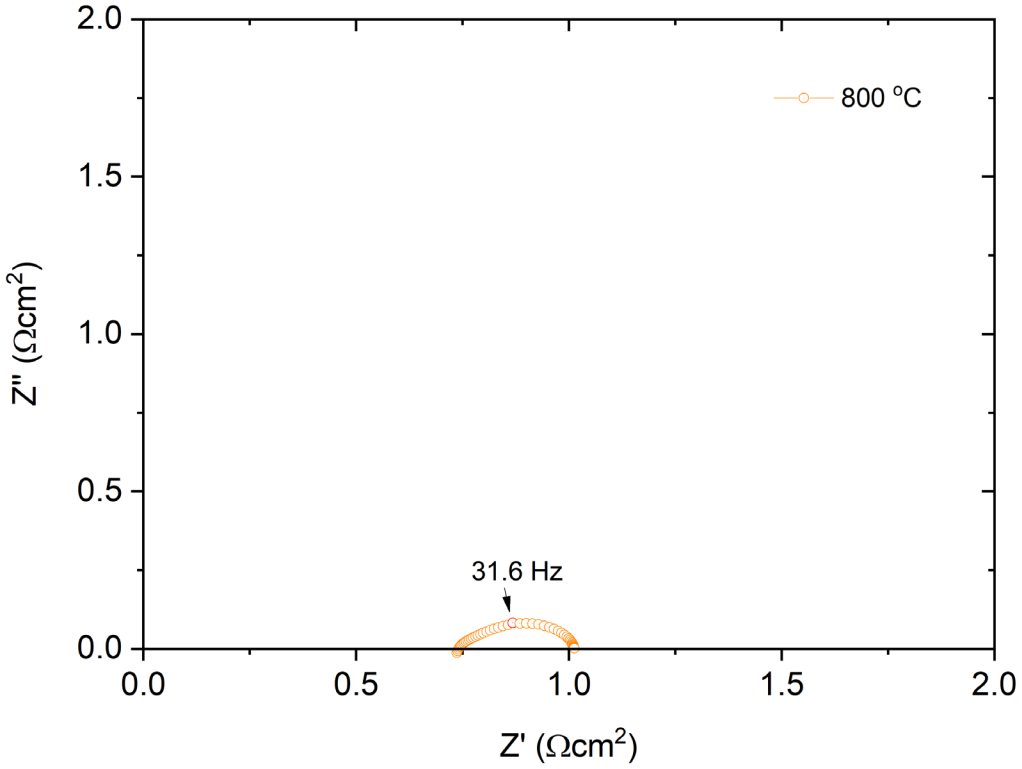

Figure S13. $(La_{0.8}Sr_{0.2})_{0.95}MnO_3$ symmetric cell test at 800 °C in air.

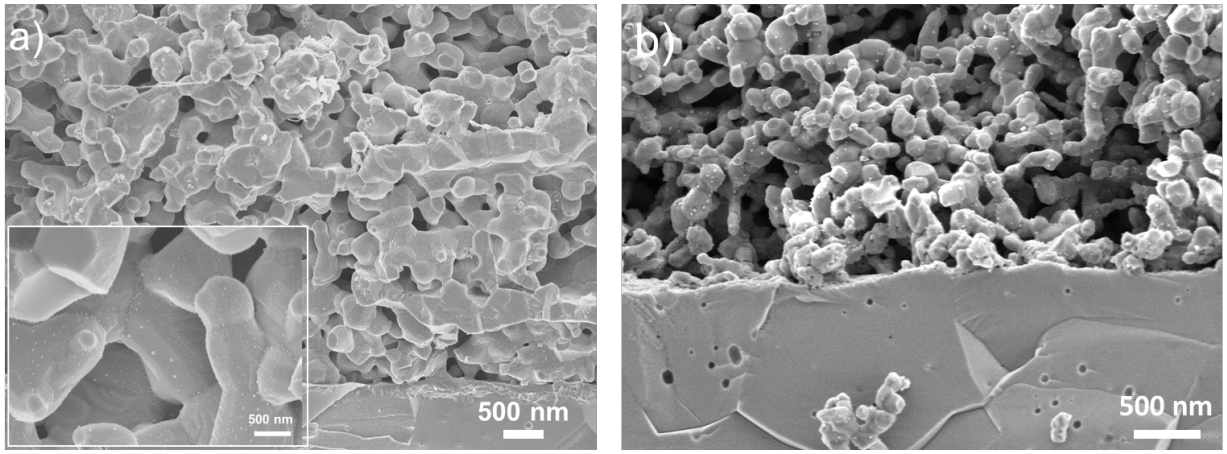

Figure S14. SEM image of magnified area for cross-section for (a) symmetric cell reduced in 5% H_2, (b) solid oxide cell after switching at 900 ℃ in wet H_2.

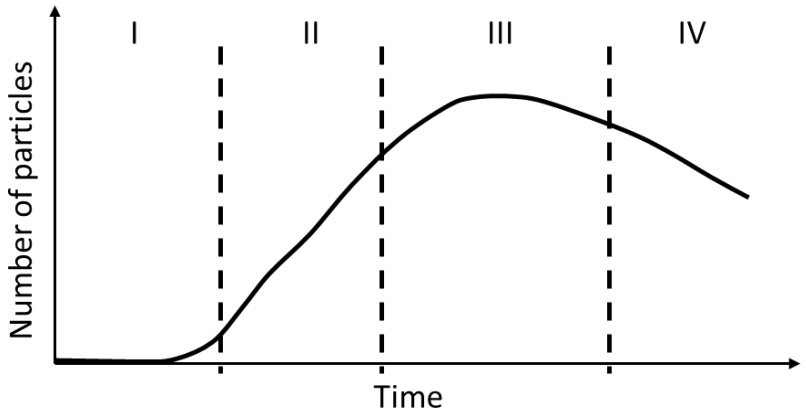

Figure S15. Number of particles formed during a discontinuous transformation, as a function of time at constant temperature.[8]

The exsolution can be described as discontinuous phase transformations that generally occur in series of states, including incubation state, quasi-steady state, nucleation expansion state and growth state[8], as shown in Fig.S10. During the quasi-steady-state nucleation stage, a spinodal decomposition process yields the nanoparticles on the surface as an unstable region driven by the negative segregation energy and low oxygen partial pressure. The number of stable particles becomes almost constant when the nucleation is complete, while the nucleated particles grow at the expense of the small particles due to the decrease in free energy.

I : incubation state, in which the new metastable phase formed without stable particles at this stage;

II : quasi-steady state, in which nucleation regime formed with building up of clusters and stable nuclei;

III : nucleation expansion state, in which the nucleation rate decreased as supersaturation/free energy decreased and driven the nucleation in untransformed regions.

IV : growth state, in which nucleation of new particles is negligible, instead, larger particles grow at the expanse of the smaller particles.

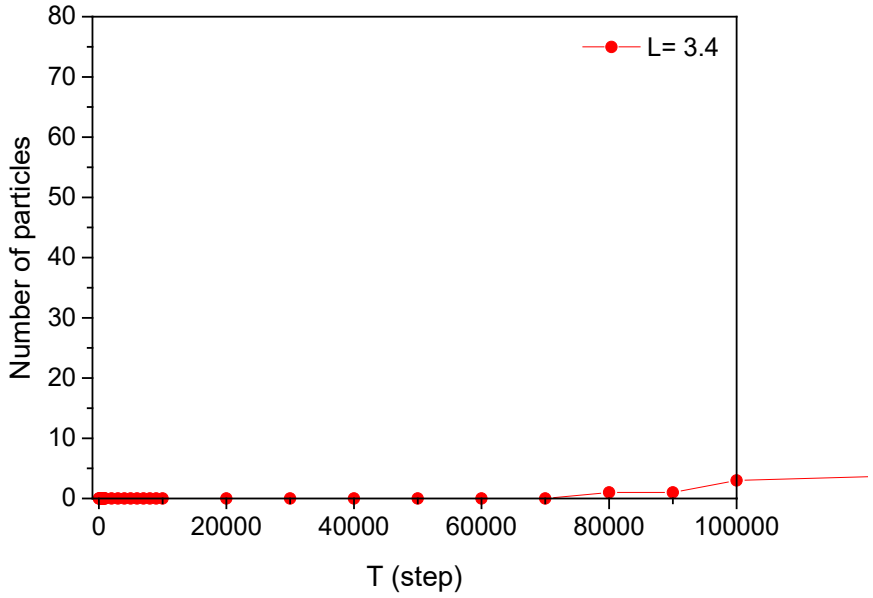

Figure S16. Phase-field simulation results for exsolution. The exsolution number of particles vs steps.

Table S1. Geometry and functional parameters used in the phase-field model.

	Symbols	Values
Radius of the perovskite	R	170
Length of the atmosphere	D	500
Gradient energy coefficients	κ_i	10
Molar fraction of P in bulk	x_P	0.9271
Molar fraction of P in atmosphere	x_P	0.0129
Molar fraction of B' in bulk	$x_{B'}$	0.06
Molar fraction of B' in atmosphere	$x_{B'}$	0.0129
Onsager coefficients of P in bulk	M_P	0.0001
Onsager coefficients of P in surface layer	M_P	0.0001
Onsager coefficients of P in atmosphere	M_P	2
Onsager coefficients of B' in bulk	$M_{B'}$	1
Onsager coefficients of B' in surface layer	$M_{B'}$	1
Onsager coefficients of B' in atmosphere	$M_{B'}$	2
Structural order parameter in bulk	η	1
Structural order parameter in atmosphere	η	-1
Segregation energy of P	μ_{P}^{seg}	0
Segregation energy of B'	$\mu_{\mathrm{B'}}^{seg}$	-0.6
Segregation energy of A	μ_{A}^{seg}	0
Interaction energies between components	L_{ij}	3.4/4.5/5.4
Radius of the circle	R	170
Length of a side of the whole model	D	500

Table S2. Results of the Rietveld refinements performed on perovskite samples prepared by different methods.

Synthesis method	Space group	Cell parameters/Å	Volume/Å^3	Rietveld parameter
Solid state	I 4 / m c m	a=b=5.4769(0), c=7.7543(8)	232.604	wR_p=7.75 R_p=6.08 Chi^2=1.07
Electrospinning	I 4 / m c m	a=b=5.4739(7), c=7.7482(89	232.173	wR_p=8.06 R_p=6.15 Chi^2=1.38

Table S3. EIS values of different fiber perovskite electrode cells under OCV in wet H_2 at different temperature.

Ω cm²		**800 °C Wet H_2**	**900 °C Wet H_2**
Before	R_s	0.64	0.86
	R_p	199.34	6.02
1.8 V	R_s	0.61	0.41
	R_p	69.77	1.10
2.0 V	R_s	0.57	0.42
	R_p	17.19	0.76
2.1 V	R_s	0.52	0.36
	R_p	9.72	0.69

References

1. Ravel, B.; Newville, M., ATHENA, ARTEMIS, HEPHAESTUS: data analysis for X-ray absorption spectroscopy using IFEFFIT. *J. Synchrotron Rad.* **2005,** *12* (4), 537-541.
2. Newville, M., EXAFS analysis using FEFF and FEFFIT. *J. Synchrotron Rad.* **2001,** *8* (2), 96-100.
3. Jiang, G., Yan, F., Wan, S., Zhang, Y. and Yan, M., Microstructure evolution and kinetics of B-site nanoparticle exsolution from an A-site-deficient perovskite surface: a phase-field modeling and simulation study. *Phys Chem Chem Phys* **2019,** *21* (21), 10902-10907.
4. Gao, Y.; Lu, Z.; You, T. L.; Wang, J.; Xie, L.; He, J.; Ciucci, F., Energetics of nanoparticle exsolution from perovskite oxides. *J. Phys. Chem. Lett.* **2018,** *9* (13), 3772-3778.
5. Kwon, O.; Sengodan, S.; Kim, K.; Kim, G.; Jeong, H. Y.; Shin, J.; Ju, Y. W.; Han, J. W.; Kim, G., Exsolution trends and co-segregation aspects of self-grown catalyst nanoparticles in perovskites. *Nat. Commun.* **2017,** *8*, 15967.
6. Gao, Y.; Chen, D.; Saccoccio, M.; Lu, Z.; Ciucci, F., From material design to mechanism study: nanoscale Ni exsolution on a highly active A-site deficient anode material for solid oxide fuel cells. *Nano Energy* **2016,** *27*, 499-508.
7. Myung, J. H.; Neagu, D.; Miller, D. N.; Irvine, J. T. S., Switching on electrocatalytic activity in solid oxide cells. *Nature* **2016,** *537* (7621), 528-531.
8. Robert W. Balluffi, S. M. A., W. Craig Carter, *Kinetics of Materials* John Wiley & Sons, Inc.: 2005.